Kinematic Modeling and Jacobian-Based Control of the COAST Guidewire Robot

Achraj Sarma, *Graduate Student Member, IEEE*, Timothy A. Brumfiel, Yash Chitalia, and Jaydev P. Desai, *Fellow, IEEE*

***Abstract*—Manual guidewire navigation and placement for minimally invasive surgeries suffer from technical challenges due to imprecise tip motion control to traverse highly tortuous vasculature. Robotically steerable guidewires can address these challenges by actuating a compliant tip through multiple degrees-of-freedom for maneuvering through vascular pathways. In this paper, we detail the kinematic mapping of a COaxially Aligned STeerable (COAST) guidewire robot that is capable of executing follow-the-leader motion in three dimensional vascular pathways. We also develop an analytical Jacobian model to perform velocity kinematics for the robot and finally, we implement Jacobian-based control to demonstrate follow-the-leader motion of the guidewire in free space, within 3D-printed phantoms, and within *ex vivo* animal vasculature.**

***Index Terms*—Medical robotics, open loop systems, robot kinematics.**

I. Introduction

ACCORDING to the American Heart Association (AHA), cardiovascular diseases (CVDs) remain the leading cause of mortality in the United States, with 49.2% of adults ≥20 years of age being affected by them [1]. Peripheral arterial disease (PAD) is a type of CVD resulting due to narrowing or blockage of blood vessels, primarily caused by build-up of plaque in the arteries. Within the United States alone, 6.5 million individuals ≥40 years of age suffer from PAD [1]. To treat PAD or similar CVDs, minimally invasive endovascular interventions have shown to improve patient mortality by offering faster recovery time, lower post-operative trauma, and decreased blood loss as compared to open surgeries [2]. Endovascular treatments involving the use of catheters are often prefaced by the placement of a long and thin "guidewire". Commercial guidewires of varying lengths and compliance are used by the surgeon to traverse vascular anatomy within the patient by using the Seldinger technique to insert the guidewire [3]. For maneuvering the device, visual feedback is often available via 2D fluoroscopy. However, the current practice suffers from several limitations. Accurate navigation of a passive wire through extreme vascular tortuosity and angulation is difficult and this is the major cause of failure in endovascular procedures [4]. Additionally, the surgeon has to rely on 2D fluoroscopic images to navigate the tool in 3D pathways. This also leads to increased radiation exposure and associated risks to the personnel and the patient in the operating room [5].

Continuum robots have become increasingly promising for minimally invasive medical procedures due to their ability to perform complex motion, inherent compliance, and significantly small scale compared to their rigid counterparts. Several different design approaches have surfaced for minimally invasive procedures [6] including shape memory alloy (SMA) actuated [7], concentric tube [8], [9], [10], magnetically steerable [11], [12], [13], and tendon driven [14], [15] robots whose goal is to improve steerability within vasculature. Precise kinematics models for continuum robots pose complications due to non-linearities in both mechanics and materials (for example, from hysteretic tendon-sheath friction, stress-strain properties of superelastic nitinol, etc.). One common approach to continuum manipulator kinematics is a piece-wise constant curvature assumption, allowing for simplified kinematics mappings [16], [17]. However, limited development of dynamic models, coupled with sensor size constraints, make feedback control of continuum manipulators at such small scales challenging. Most control approaches consist of open loop control of the end-effector through precise actuator control and mechanics based forward mappings. Several control strategies utilize EM trackers [18], or vision-based feedback [19], [20]. Our prior work detailed the design of the COAST guidewire robot and the ability to control the bending length and the radius of curvature of the distal tip [21]. We also utilized fluoroscopic imaging for the COAST guidewire path planning [22]. Using an improved compact actuation mechanism for the COAST guidewire robot with torquing capability (see Section II-B), the primary contributions of this paper include the modeling and detailed validation of the motion of the COAST guidewire robot, enabled through a Jacobian-based control scheme derived from the product of exponentials formulation of the forward kinematics. The guidewire is maneuvered in free space, within

Manuscript received 8 June 2022; revised 16 August 2022; accepted 13 October 2022. Date of publication 20 October 2022; date of current version 21 November 2022. This article was recommended for publication by Associate Editor S. Wang and Editor P. Dario upon evaluation of the reviewers' comments. This work was supported in part by the National Heart, Lung, and Blood Institute of the National Institutes of Health under Award R01HL144714. The content is solely the responsibility of the authors and does not necessarily represent the official views of the National Institutes of Health. *(Corresponding author: Timothy A. Brumfiel.)*

Achraj Sarma is with the Medical Robotics and Automation Laboratory, Wallace H. Coulter Department of Biomedical Engineering, Georgia Institute of Technology, Atlanta, GA 30332 USA.

Timothy A. Brumfiel and Jaydev P. Desai are with the Medical Robotics and Automation Laboratory, Wallace H. Coulter Department of Biomedical Engineering, Georgia Institute of Technology, Atlanta, GA 30332 USA (e-mail: tbrumfiel3@gatech.edu).

Yash Chitalia was with the Medical Robotics and Automation Laboratory, Wallace H. Coulter Department of Biomedical Engineering, Georgia Institute of Technology, Atlanta, GA 30332 USA. He is now with Boston Children's Hospital, Harvard Medical School, Boston, MA 02115 USA.

Digital Object Identifier 10.1109/TMRB.2022.3216026

constrained 3D printed phantoms, within anatomic 3D printed vascular phantoms and within an *ex vivo* animal vasculature setup. For each trial, we analyze the guidewire motion, the final tip position and present our conclusions.

This paper is organized as follows: We first summarize the mechanical designs in Section II for the COAST guidewire robot (Section II-A) and the compact actuation mechanism (Section II-B), followed by brief overview of the joint kinematics (Section II-C). In Section III, we develop the forward kinematics model (Section III-A) and a Jacobian-based inverse kinematics model (Section III-B) for the COAST robot to generate joint inputs, given a follow-the-leader (FTL) trajectory. A control scheme is presented involving feedforward and feedback blocks to compensate for joint space errors (Section III-C). In Section IV, we implement this scheme for the COAST robot for experiments to perform FTL motion in free space (Section IV-A). We also demonstrate the motion of the robot within 3D printed phantoms (Section IV-B), within 3D printed anatomical vascular phantoms (Section IV-C), and within *ex vivo* animal vasculature (Section IV-D). Finally, we present our conclusions in Section V.

II. Mechanical Design and Model

A. COAST Guidewire

The components of the COAST guidewire are shown in Fig. 1(a), consisting of a notched nitinol outer tube, a notched nitinol middle tube, a stainless-steel inner tube, and a single nitinol tendon. The guidewire structure can be divided into a bending segment, consisting of coaxially aligned outer and middle tubes such that their respective notches are 180° out of phase, and a non-bending segment, consisting of all three tubes and the tendon. The location of the inner tube controls the length of the bending segment by adding stiffness from the proximal side. Rectangular unidirectional asymmetric notch patterns are micromachined on the superelastic nitinol tubes using a femtosecond laser (WS-Flex Ultra-Short Pulse Laser Workstation, Optec, Frameries, Belgium). The middle and outer tubes of the guidewire develop pre-curvatures induced by asymmetric heating during the laser micromachining process. However, the notch depths of the middle and outer tubes are selected such that, when combined, the assembly's pre-curvature is minimized, resulting in an approximately straight unactuated configuration. The relevant notch dimensions are illustrated in Fig. 1(b). The nitinol tendon, soldered at the tip to fix it to the distal end of the middle tube, is routed through the inner tube and out of the proximal end of this combined assembly (a detailed description of the structure is presented in [21]). Table I highlights the relevant dimensions and properties of the tubes and the tendon used for this study (Young's moduli of the tubes are estimated with the joint kinematics model in Section II-C, and that of the tendon is found in [21]).

B. Compact Actuation System (CAS)

The compact actuation system (CAS) is a cylindrical mechanism of length 165.11 mm and diameter 41 mm. The CAS, affixed to an actuator stage, is linearly translated using a DC Motor (Pololu Robotics and Electronics, NV, United States) and a lead-screw combination, with linear-bearing rails (McMaster-Carr, GA, USA) for support. Rolling motion of the CAS is achieved with a DC motor (Maxon Precision Motors, MA, United States) attached to a spur gear, allowing for tip bending in 3D space. The outer tube, inner tube, and tendon of the COAST guidewire are actuated by DC motors (Maxon Precision Motors, MA, United States) with a lead screw assembly, while the middle tube is rigidly secured to the CAS. Each lead-screw is supported on both ends through locating and non-locating bearings, mitigating the affects of radial and axial misalignment. The actuation stage and the CAS mechanism are shown in Figs. 2(a) and 2(b), respectively. The CAS and the actuation stage offer improvements over our previous design [21] by increasing the insertion/retraction length to 375 mm (2.5 times the previous length) and by adding roll motion capability. Considering each motor, there are five controllable variables that can be summarized as:

$$\begin{bmatrix} \psi \\ X_t \\ X_b \\ X_e \\ X_s \end{bmatrix} = \begin{bmatrix} \text{Roll Angle} \\ \text{Tendon Stroke} \\ \text{Bending Segment Length} \\ \text{Outer Tube Displacement} \\ \text{Actuator Stage Displacement} \end{bmatrix}$$

The COAST mechanism features two modes of operation:

- Follow-the-leader (FTL) motion: FTL motion can be achieved by controlling X_t, X_b and X_s simultaneously at any roll angle $\psi \in (-\pi, \pi]$.

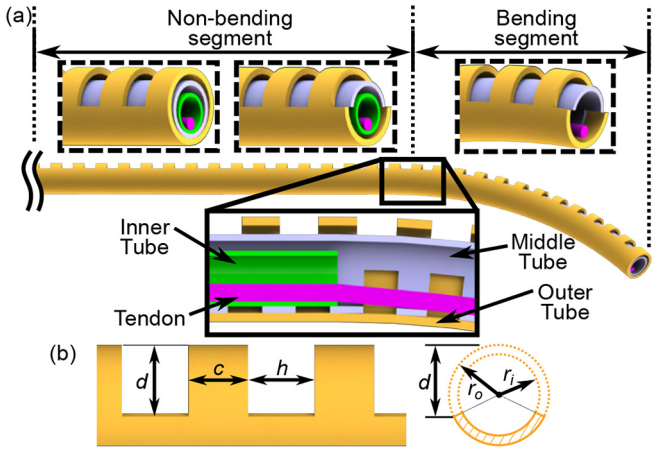

Fig. 1. (a) Structure of the COAST guidewire showing arrangement of tubes and tendon in the non-bending and bending sections, (b) Schematic showing notch parameters on the micromachined nitinol tubes.

TABLE I
Specifications of the COAST Guidewire Prototype

Items	Outer tube	Middle tube	Inner tube	Tendon
Total length (mm)	242.00	253.10	269.50	388.68
Length of the notched section (mm)	112.8	75.0	-	-
Outer diameter, $2r_o$, (mm)	0.480	0.360	0.254	0.076
Inner diameter, $2r_i$, (mm)	0.400	0.300	0.239	-
Notch depth, d (mm)	0.400	0.243	-	-
Notch width, h (mm)	0.315	0.315	-	-
Notch spacing, c (mm)	0.285	0.285	-	-
Young's modulus (GPa)	42.600	42.600	200	53.965

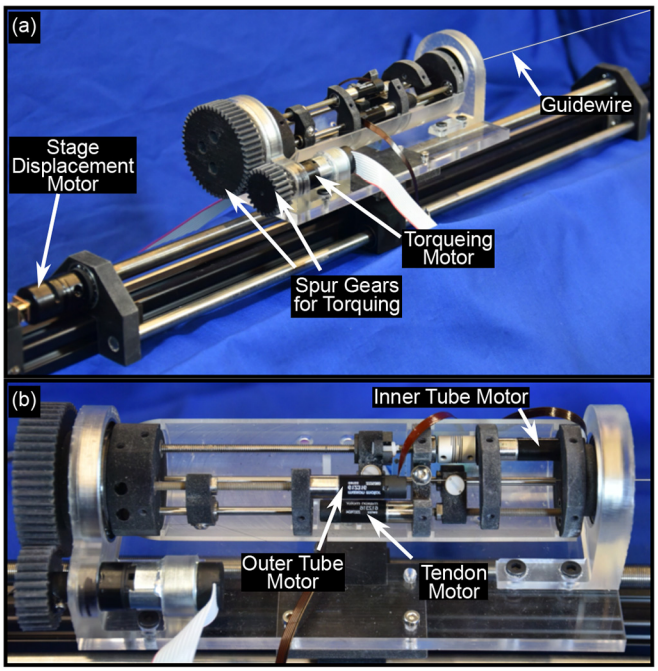

Fig. 2. (a) Compact actuation system (CAS) fixed on actuator stage, displaced using a motor-lead screw assembly and rolled using the torquing motor-spur gear assembly, (b) Image of inner mechanism of the CAS, showing the motors and lead screws for actuating the tubes and tendon.

- Extended-feed (ExF) motion: The outermost tube can be individually advanced (by actuating X_e) to further displace the distal tip of the robot while retaining the current curvature along the body of the robot.

As ExF motion involves only the outer tube displacement, it can be used to advance the tip of the robot to a location that may have been inaccessible with only an FTL maneuver.

C. Joint Kinematics and Statics Model

The motion of the bending segment of the guidewire in terms of the tendon stroke, X_t, bending length, X_b and the desired curvature, κ, is derived as:

$$X_t = \underbrace{\Delta L^{kin}(\kappa, X_b)}_{\text{Geometric Stroke}} + \underbrace{\frac{E(I_{out}+I_{mid})L_{total}}{\Delta y_t E_t \pi r_t^2}\kappa}_{\text{Tendon Elongation}} \quad (1)$$

The expressions for the geometric stroke and the tendon elongation terms are detailed in [21]. Tendon elongation dominates the relationship and is characterized by the Young's modulus of the nitinol tubes (E), the length of the tendon (L_{total}), the tendon wire radius (r_t), the Young's modulus of the nitinol tendon wire (E_t), the moment arm of the tendon at the tip (Δy_t), and the second moments of area of the middle and outer tubes (I_{mid} and I_{out}, respectively).

The friction loss due to the interaction of the tendon with the notches of the middle tube (each notch wall is assumed to contribute the same amount towards the friction loss), when actuating the bending segment, is modeled as an exponential relation, η^{N_f}, based upon the work presented in [23]. η represents the coefficient of friction while the exponent, N_f, represents the number of notch corners and is determined as

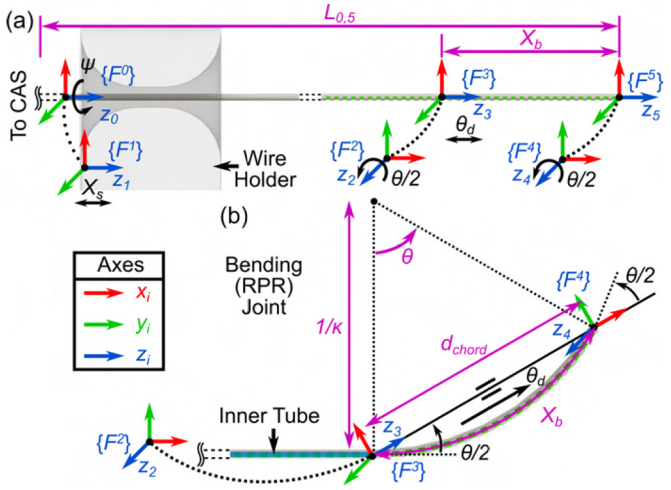

Fig. 3. Schematic of (a) unactuated COAST guidewire showing the coordinate frames $\{F^0\}$-$\{F^5\}$ (x, y and z axes shown with red, green, and blue arrows, respectively), and (b) bending joint at the guidewire tip considered as a serial RPR manipulator (Frames $\{F^2\}$, $\{F^3\}$, and $\{F^4\}$ correspond to the first revolute (R), prismatic (P), and second revolute (R) joints, respectively).

$N_f = (X_b N_{mid})/L_{mid}^{notch}$ (N_{mid} is the number of notches and L_{mid}^{notch} is the length of the notched section for the middle tube). Furthermore, the tendon wire is routed around two pulleys inside the CAS (allowing for a compact motor-lead screw arrangement). To account for the friction interaction of the tendon and the pulleys, we use the Capstan friction equation, $e^{\mu\alpha}$, where μ is the coefficient of friction and $\alpha = \pi$ is the pulley wrapping angle [6]. The modified joint kinematics and statics model is given by:

$$X_t = \underbrace{\Delta L^{kin}(\kappa, X_b)}_{\text{Geometric Stroke}} + \underbrace{e^{\mu\alpha}\eta^{N_f}}_{\text{Friction Loss}} \underbrace{\frac{E(I_{out}+I_{mid})L_{total}}{\Delta y_t E_t \pi r_t^2}\kappa}_{\text{Tendon Elongation}} \quad (2)$$

Similar to [21], we validate the model given in Eq. (2) by observing the tendon stroke vs. curvature data for constant bending lengths. The values of the coefficients of friction, $\mu = 0.2965$ and $\eta = 1.0063$, were estimated from the validation results by manually calibrating the parameters to fit the joint model to the experimental data. The Young's modulus of the tubes, $E = 42.6$ GPa, was also varied between the vendor specified values ($40 \sim 45$ GPa). These estimates for μ, η and E are used in the joint model, which is in turn used for the motion control of the robot.

III. Kinematics and Control

A. COAST Robot Forward Kinematics

We now define a Forward Kinematics (FK) map for the COAST guidewire robot, and use an analytical Jacobian to map the joint space velocity, $\dot{\boldsymbol{q}}$, of the robot to the Cartesian space velocity, $\dot{\boldsymbol{x}}$. We consider frames $\{F^i\}$, $i = \{0, 1, 2, 3, 4, 5\}$, shown in Fig. 3(a) for the robot joints, and use the product of exponentials to define the transformation from the tool-frame, $\{F^5\}$, to the base-frame, $\{F^0\}$. The frames $\{F^0\}$-$\{F^5\}$ are positioned on the robot as follows: $\{F^0\}$ and $\{F^1\}$ reside at the proximal end of the robot, $\{F^2\}$ and $\{F^3\}$

are located at the beginning of the bending segment (length X_b before the robot tip), and finally, $\{F^4\}$ and $\{F^5\}$ coincide with the tip of the robot (i.e., the end of the bending segment). The transformation between the base and tool-frames of the unactuated COAST robot and is given by:

$$g_{st}(0) = \begin{bmatrix} 1 & 0 & 0 & 0 \\ 0 & 1 & 0 & 0 \\ 0 & 0 & 1 & L_{0,5} \\ 0 & 0 & 0 & 1 \end{bmatrix} \tag{3}$$

where $L_{0,5}$ is the constant distance measured between the CAS exit and the distal tip of the robot. As in our earlier work [21], we assume a constant curvature bending characterized by κ. The bending length is defined by X_b and bending angle is then given as $\theta = \kappa X_b$. The remaining joint parameters are defined as the stage displacement, X_s, and the roll (torquing) angle, ψ. The constant curvature bend can be represented geometrically as a chord (shown in Fig. 3(b)). The tangent angles of the chord are defined as half of the bending angle whereas the change in length, θ_d, is defined as the difference between chord and arc length, and is given by:

$$\theta_d = d_{chord} - X_b = \frac{2X_b \sin(\theta/2)}{\theta} - X_b \tag{4}$$

Thus, the bending joint can be modeled as a revolute-prismatic-revolute (RPR) joint [16] with parameters $\theta/2$, θ_d, and $\theta/2$ shown in frames $\{F^2\}$, $\{F^3\}$, and $\{F^4\}$ respectively.

The twist for joint i is defined as $\xi_i = \begin{bmatrix} v_i & \omega_i \end{bmatrix}^T$, where ω_i is the unit angular velocity of the joint as expressed in the fixed frame, and $v_i = -\omega_i \times q_i$, with q_i being the position vector associated with a point on the axis of rotation in frame $\{F^i\}$, with respect to base frame $\{F^0\}$ [24]. The twist for a prismatic joint is defined as $\xi_i = \begin{bmatrix} v_i & 0 \end{bmatrix}^T$, where v_i is the unit velocity of the origin of the frame $\{F^i\}$ affixed to the prismatic joint. The angular velocities and the position vectors of the frames for the revolute joints are given by:

$$\begin{aligned} &\omega_1 = \begin{bmatrix} 0 & 0 & 1 \end{bmatrix}^T,\ \omega_3 = \begin{bmatrix} 0 & 1 & 0 \end{bmatrix}^T, \omega_5 = \begin{bmatrix} 0 & 1 & 0 \end{bmatrix}^T \\ &q_1 = \begin{bmatrix} 0 & 0 & 0 \end{bmatrix}^T,\ q_3 = \begin{bmatrix} 0 & 0 & (L_{0,5} - X_b) \end{bmatrix}^T, \\ &q_5 = \begin{bmatrix} 0 & 0 & L_{0,5} \end{bmatrix}^T \end{aligned} \tag{5}$$

The linear velocities for the frames affixed to the prismatic joints are given as:

$$v_2 = \begin{bmatrix} 0 & 0 & 1 \end{bmatrix}^T,\ v_4 = \begin{bmatrix} 0 & 0 & 1 \end{bmatrix}^T \tag{6}$$

The resultant twists for each joint are given by:

$$\begin{aligned} &\xi_1 = \begin{bmatrix} 0 & 0 & 0 & 0 & 0 & 1 \end{bmatrix}^T, \xi_2 = \begin{bmatrix} 0 & 0 & 1 & 0 & 0 & 0 \end{bmatrix}^T, \\ &\xi_3 = \begin{bmatrix} -(L_{0,5} - X_b) & 0 & 0 & 0 & 1 & 0 \end{bmatrix}^T, \\ &\xi_4 = \begin{bmatrix} 0 & 0 & 1 & 0 & 0 & 0 \end{bmatrix}^T, \\ &\xi_5 = \begin{bmatrix} -(L_{0,5}) & 0 & 0 & 0 & 1 & 0 \end{bmatrix}^T \end{aligned} \tag{7}$$

The FK map of the robot is given through the product of exponentials [24]:

$$g_{st}(\Theta) = e^{\hat{\xi}_1 \psi} e^{\hat{\xi}_2 X_s} e^{\hat{\xi}_3 \frac{\theta}{2}} e^{\hat{\xi}_4 \theta_d} e^{\hat{\xi}_5 \frac{\theta}{2}} g_{st}(0) \tag{8}$$

After substituting Eq. (3) and Eq. (7) into Eq. (8), we obtain the forward kinematics mapping (using S and C denote the sine and cosine functions respectively) as:

$$g_{st}(\Theta) = \begin{bmatrix} C_\psi C_\theta & -S_\psi & C_\psi S_\theta & C_\psi \frac{1-C_\theta}{\kappa} \\ S_\psi C_\theta & C_\psi & S_\psi S_\theta & S_\psi \frac{(1-C_\theta)}{\kappa} \\ -S_\theta & 0 & C_\theta & \frac{S_\theta}{\kappa} + L_{0,5} - X_b + X_s \\ 0 & 0 & 0 & 1 \end{bmatrix} \tag{9}$$

The position, $\boldsymbol{p} = (p_x, p_y, p_z)$, of the guidewire tip is given by the fourth column, while the orientation of the tangent vector at the tip, $\boldsymbol{t} = (t_x, t_y, t_z)$, is given by the third column of the matrix $g_{st}(\Theta)$. The Cartesian space is then defined by $\boldsymbol{x} = [p_x\ p_y\ p_z\ t_x\ t_y\ t_z]^T$. We make a note here that the ExF motion (X_e) is treated as an additional feature of the COAST guidewire mechanism and not included in the kinematic mapping. The joint space hence consists of the inputs $\boldsymbol{q} = [\psi\ X_t\ X_b\ X_s]^T$. Modeling and control with X_e as input for trajectories involving FTL-inaccessible targets will be included in our future work.

B. Jacobian Model

Given a constant curvature trajectory, the joint input required to achieve the desired trajectory is estimated using the Jacobian pseudo inverse ($J^\dagger$). We begin with the mapping of the joint input velocity vector, $\dot{\boldsymbol{q}} = [\dot{\psi}\ \dot{X}_t\ \dot{X}_b\ \dot{X}_s]^T$, onto the Cartesian space velocity vector, $\dot{\boldsymbol{x}} = [\dot{p}_x\ \dot{p}_y\ \dot{p}_z\ \dot{t}_x\ \dot{t}_y\ \dot{t}_z]^T$.

$$\dot{\boldsymbol{x}} = J(\boldsymbol{q})\dot{\boldsymbol{q}} \tag{10}$$

where $J(\boldsymbol{q})$ is the analytical Jacobian matrix formed by the partial derivatives $\partial \boldsymbol{x}/\partial \boldsymbol{q}$.

The FK map $g_{st}(\Theta)$ (Eq. (9)) does not show the direct dependence of the trajectory on the joint variable X_t. To obtain the kinematics pertaining to X_t, we consider the time derivative of the kinematic model (Eq. (2)):

$$\dot{X}_t = \frac{\partial X_t}{\partial X_b}\dot{X}_b + \frac{\partial X_t}{\partial \kappa}\dot{\kappa} \tag{11}$$

Hence, Eq. (11) allows us to compute the rate of change of tendon stroke, X_t, in terms of rates of change of bending length, X_b, and the curvature, κ. We then redefine the joint space as $\boldsymbol{q'} = [\psi\ X_b\ X_s]^T$ and $J(\boldsymbol{q'})$ as:

$$J(\boldsymbol{q'}) = \begin{bmatrix} \frac{\partial \boldsymbol{x}}{\partial \psi} & \frac{\partial \boldsymbol{x}}{\partial X_b} & \frac{\partial \boldsymbol{x}}{\partial X_s} \end{bmatrix} = \begin{bmatrix} -S_\psi \frac{1-C_\theta}{\kappa} & C_\psi S_\theta & 0 \\ C_\psi \frac{1-C_\theta}{\kappa} & S_\psi S_\theta & 0 \\ 0 & C_\theta - 1 & 1 \\ -S_\psi S_\theta & \kappa C_\psi C_\theta & 0 \\ C_\psi S_\theta & \kappa S_\psi C_\theta & 0 \\ 0 & -\kappa S_\theta & 0 \end{bmatrix} \tag{12}$$

A full column rank Jacobian matrix results in an overdetermined system. To obtain the Inverse Kinematics (IK), we consider a general least squares solution to Eq. (10), resulting in the left pseudo inverse, $J^\dagger$, and the solution for $\dot{\boldsymbol{q}}'$ is:

$$\dot{\boldsymbol{q}}' = J^\dagger \dot{\boldsymbol{x}},\ \text{where } J^\dagger = \left(J^T J\right)^{-1} J^T \tag{13}$$

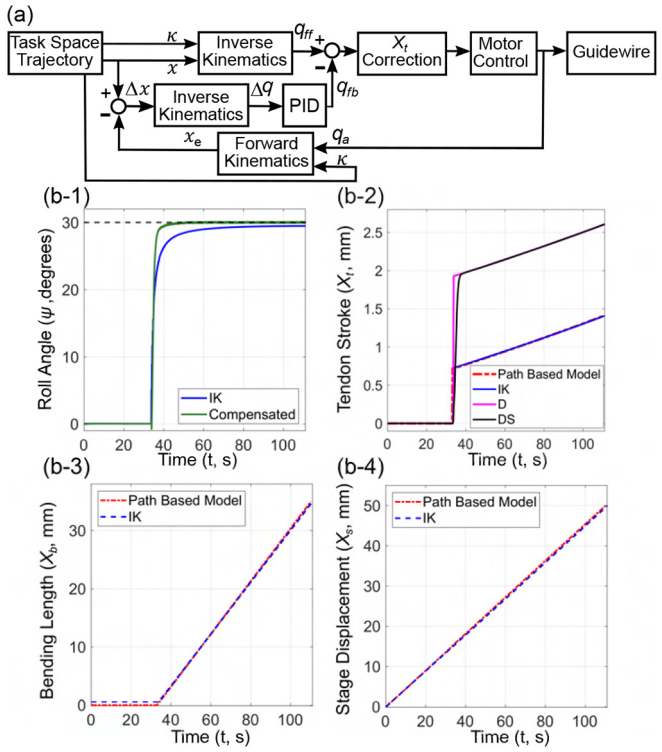

Fig. 4. (a) Cartesian space trajectory control block diagram, and plots showing (b-1) ψ, (b-2) X_t, (b-3) X_b, and (b-4) X_s for trajectory $T_{1,30^\circ}$.

The obtained $\dot{\boldsymbol{q}}'$ vector is then integrated to find the inputs ψ, X_b, and X_s, each as a function of time. Using Eq. (11), $\dot{X}_t$ is integrated similarly to find X_t. This completes the solution for $\boldsymbol{q} = [\psi \ X_t \ X_b \ X_s]^T$, for a given constant curvature trajectory. Typical trajectories encountered by the guidewire robot within vasculature may be sectioned into successive pairs of constant curvature paths which may be preceded by straight paths. For the straight path of a trajectory section, the robot's configuration results in the Jacobian matrix $J(\boldsymbol{q}')$ losing rank ($\kappa = 0$ in Eq. (12)). An analytical solution for the joint space in this case is easily determined, hence the IK solution is only applied for the curved paths of the trajectory.

C. Jacobian-Based Control Implementation

The control scheme for tracking a Cartesian space trajectory, $\boldsymbol{x}$, is shown in Fig. 4(a). The feedforward term, $\boldsymbol{q_{ff}}$, is computed directly from the IK solution (defined in Section III-B), while the feedback term, $\boldsymbol{q_{fb}}$, is generated by an inverse Jacobian-based control scheme [25] due to the lack of feedback of the guidewire's Cartesian space configuration. Since both the FK and IK maps rely on the path's curvature at a given time, the trajectory also feeds the desired path curvature, κ, into each block. The feedback controller maps the estimated Cartesian space error, $\Delta\boldsymbol{x}$, to a joint space error, $\Delta\boldsymbol{q}$, with the same least squares IK solution. This is then passed through a PID controller to generate the feedback term. The least squares IK solution for X_t, X_b and X_s show negligible error when compared to the path-based control implemented in [21], while ψ is observed to show a notable joint error. This can be seen from Fig. 3 (b-1)-(b-4) where the IK solution tracks a path-based control closely. While PID gains can be applied to each joint variable, we apply non-zero gains only for ψ to reach the desired trajectory in this paper.

The kinematics model (Eq. (2)) does not account for the pre-tensioning of the tendon, resulting in an observed deadband associated with tendon stroke, X_t. This results in the IK solution producing an initial stroke length that is less than that needed to initiate bending during the transition from the straight to the curved paths of the trajectory. To compensate for this, an offset, X_{tD}, which is experimentally determined from the curvature-tendon stroke tests, is added at the transition phase for X_t. The sudden increase in X_t at the transition may result in breaking of the tendon, so the input is smoothed by scaling with the result of a sigmoid function that is shifted by a chosen Δt from the start of the transition phase. The final commanded tendon stroke, X_{tDS}, sent to the actuator is given by:

$$X_{tDS} = \frac{X_{tff} + X_{tD}}{1 + e^{-(t-\Delta t)}} \tag{14}$$

The result of deadband correction and smoothing are displayed in Fig. 4(b-2), denoted by D and DS respectively. Once generated, the combined feedback and feedforward joint space commands are sent to the motor control plant, which includes a PID controller and a Disturbance Observer [26] and finally to the motors.

IV. Experiments and Results

A. Free Space Implementation

The aforementioned control scheme is implemented for the COAST guidewire robot at an operating frequency of 500 Hz. We generate three sets of trajectories, characterized by $\{a, \delta, \theta, \psi\}$, composed of an initial straight path of length, a, followed by a constant curvature path defined by its radius of curvature, δ, bending angle, θ, and roll angle ψ (see Fig. 5(a)). Each trajectory, $T_{j,\psi}$, $j \in \{1, 2, 3\}$, is traversed with a FTL motion by the robot, first in the base plane ($\psi = 0^\circ$), and then in torqued plane ($\psi \neq 0^\circ$). The experimental torquing angle for each $T_{j,0^\circ}$-$T_{j,\psi}$ pair is acquired by computing best fit planes using singular value decomposition (SVD) of the recorded trajectory coordinates. The defined trajectories ($T_{j,0^\circ}$) and executed tip motion in the base plane are shown in Fig. 5(b-1)-(b-3). The defined trajectories and executed tip motion for torqued planes ($\psi \neq 0^\circ$), along with the estimated torquing angles, are shown in Fig. 5(c-1)-(c-3).

Significant deviations in the actual tip positions and the generated trajectories are observed in the curved path and we see a shift at the transition between the straight and curved paths for the trajectories, especially for those with larger curvatures. As addressed in our previous work [21], these are attributed to inter-segment coupling, which would be partially compensated when traversing constrained vasculature. At the transition phase, a trajectory offset to compensate for this coupling is shown for each $T_{j,0^\circ}$ to estimate the final position error of the tip, $\Delta\varepsilon_j$ (values shown in Table II for the desired path parameters, a, δ_g, and θ, measured radius of curvature, δ_m, and the

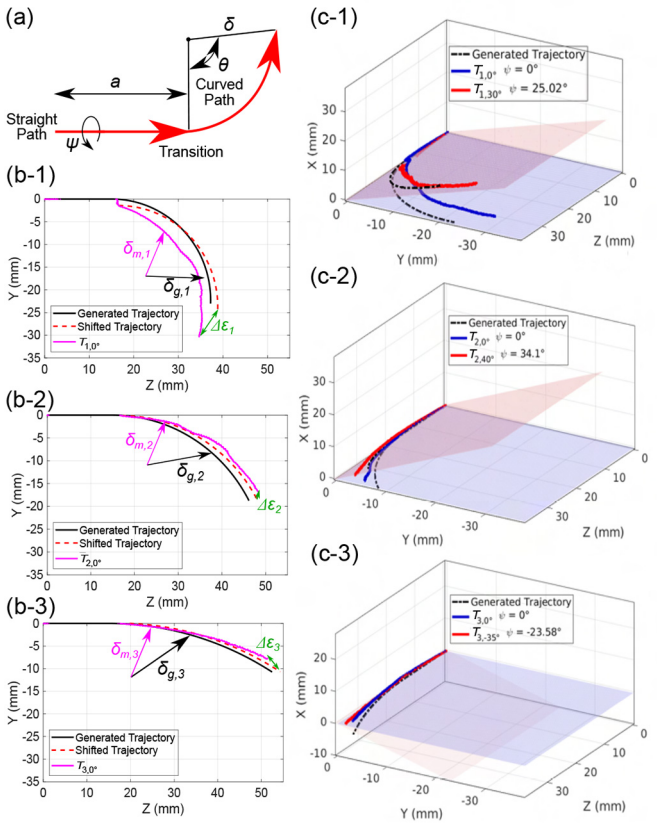

Fig. 5. (a) Schematic showing a general trajectory with straight and curved path parameters; Generated, executed and coupling compensated trajectories (b-1) $T_{1,0^\circ}$, (b-2) $T_{2,0^\circ}$, and (b-3) $T_{3,0^\circ}$; Generated and executed trajectories, and best fit planes for (c-1) $T_{1,0^\circ}$ (blue), $T_{1,30^\circ}$ (red), (c-2) $T_{2,0^\circ}$ (blue), $T_{2,40^\circ}$ (red), (c-3) $T_{3,0^\circ}$ (blue), $T_{3,-35^\circ}$ (red).

TABLE II
TRAJECTORY PARAMETERS AND TRACKING RESULTS FOR FREE AIR TRIALS

Trajectory	Straight Path	Curved Path		Measured Radius	Final Tip Error
	a (mm)	δ_g (mm)	θ°	δ_m (mm)	$\Delta\varepsilon$ (mm)
$T_{1,0^\circ}$	15	22.24	90	24.05	8.46
$T_{2,0^\circ}$	15	35.33	60	33.44	3.26
$T_{3,0^\circ}$	15	70.67	30	92.82	4.29

tip position error, $\Delta\varepsilon_j$). The average tip positioning error per unit length of the guidewire robot ($L_{0,5} = 190$ mm), for all of the free air trials, is 2.81%, showing acceptable performance compared to the kinematic modeling of the tendon-driven continuum robots presented in [27] and [15], which present errors per length of 2.72% and 2.88%, respectively.

Further deviations, specifically in the torquing angle, result due to mechanical backlash in the torquing gears, as well as the weight of the EM tracker and the connecting wire, which apply a moment at the tip and deflect the robot from the intended trajectory. The deviation worsens for higher commanded torquing angles as the connecting wire interferes with torquing motion at the tip by resisting the motion or inducing vibrations. The results of planar tracking for the trajectory $T_{1,0^\circ}$ (parameters specified in Table II, namely $a = 15$ mm, $\delta_g = 22.24$ mm, and $\theta = 90^\circ$) with a CMOS camera (Zelux^{TM} 1.6 MP, Thorlabs

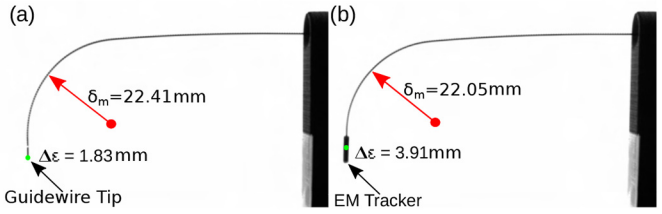

Fig. 6. Images of trajectory $T_{1,0^\circ}$ executed (a) without and (b) with the 5-DoF EM tracker.

Inc., NJ, United States) without and with the EM tracker are shown in Fig. 6(a) and Fig. 6(b), respectively, where we show the error of the guidewire tip position, $\Delta\varepsilon$, and the measured radius of curvature, δ_m.

In the trial without the EM tracker, the guidewire was visually observed to be parallel to the camera at all times, resulting in significantly less error than that shown in Table II for $T_{1,0^\circ}$ (where all of the measured data was with the EM tracker attached to the guidewire tip). The same trajectory carried out with the EM tracker attached results in visually obvious out-of-plane motion potentially caused by interference with the sensor's connecting wire. It is important to note that due to the variability of the EM tracker wire motion in free space, when the EM tracker is attached to the guidewire tip, we observe a different error in Fig. 6(b) ($\Delta\varepsilon = 3.91$ mm) compared to the data for the same desired trajectory, $T_{1,0^\circ}$, in Table II ($\Delta\varepsilon = 8.46$ mm). Hence, from the results above, we are unable to draw any quantitative conclusions regarding the EM tracker's full influence on the guidewire's tip position error. Given the invasive nature of the EM sensor system on the final tip position error, multiple camera-based imaging systems will be considered in our future work, as an alternative to track the guidewire tip and characterize the motion of the robot.

B. Navigation in Constrained 3D Phantoms

To test the FTL motion of the COAST guidewire within constrained vascular environments, the guidewire is maneuvered within a 3D printed phantom structure (Form3, Formlabs Inc., MA, USA). To observe the guidewire within the phantom, we use the OEC 9800 Plus C-Arm system (GE Healthcare®, Chicago, USA) in which images are acquired using an Orion HD (Matrox^{TM}, Dorval, Canada) frame-grabber in tandem with the MATLAB Image Acquisition Toolbox (MathWorks^{TM}, Natick, USA). The C-Arm system is used only for observing the motion of the guidewire and not used for tracking the guidewire tip or shape in this work. The phantom is placed under the C-Arm system with the guidewire positioned near the start point of each trajectory within the phantom (see Fig. 7(a), with curved paths in different bending planes (see Fig. 7(a)(inset)). The parameters of the straight and curved paths of each trajectory in the phantom are given in Table III, and the diameters of the vessels in the phantom were chosen to be 3.5 mm, which approximates the average coronary artery diameter [28]. The task space is generated based on the trajectory parameters and given as input to the Jacobian-based control scheme. Fig. 7(b-1)-(b-3) show the traversal of the COAST guidewire through trajectory 1

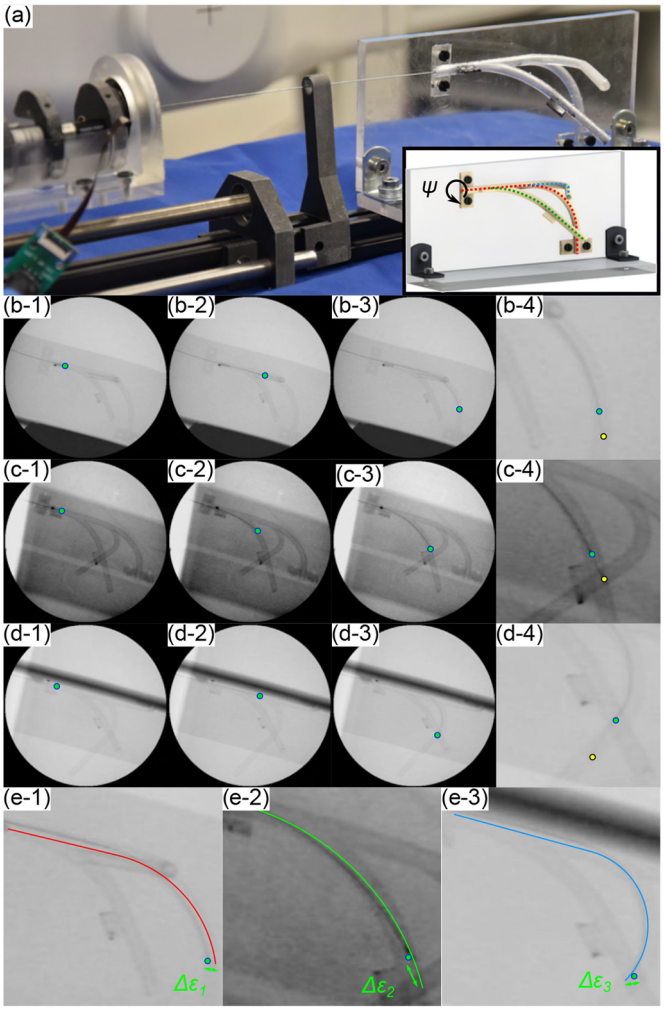

Fig. 7. (a) Experimental setup showing CAS with COAST guidewire and the 3D printed constrained vascular phantom (inset: Illustration of the three trajectories within the phantom, shown with red, green and blue dotted lines); Experimental results shown by fluoroscopy images of guidewire motion for (b-1)-(b-3) trajectory 1, (c-1)-(c-3) trajectory 2, and (d-1)-(d-3) trajectory 3 (guidewire tip marked with green dots); ExF motion for (b-4) trajectory 1, (c-4) trajectory 2, and (d-4) trajectory 3 (Outer tube tip marked with yellow dots); The final positions compared to the desired trajectory for (e-1) trajectory 1, (e-2) trajectory 2, and (e-3) trajectory 3.

(red), with the robot tip marked by green dots. Once the FTL motion is completed, ExF motion of 5 mm is performed and is marked by yellow dots. Similarly, traversal and ExF motions for trajectories 2 (green) and 3 (blue) are shown in Fig. 7(c-1)-(c-4) and 7(d-1)-(d-4), respectively. The position of the tip of the guidewire is manually determined from the image data for each trajectory shown in Fig. 7(e-1)-(e-3). The estimates of the final tip position errors for the FTL motions, with respect to the generated trajectories, are shown in Table III. The values are manually calculated from 2D image data taken using the C-Arm system with the imaging plane oriented parallel to the plane of bending (0° plane is taken as the vertical). The COAST guidewire demonstrates the ability to traverse bifurcations within 3D vasculature and perform FTL motion within constant curvature segments. ExF motion is demonstrated to further expand the reach of the robot tip. The errors are mainly

TABLE III
TRAJECTORY PARAMETERS AND TRACKING RESULTS FOR CONSTRAINED PHANTOM TRIALS

Trajectory	Straight Path	Curved Path		Torquing Angle	Final Tip Error
	a (mm)	δ (mm)	θ°	ψ°	$\Delta\varepsilon$ (mm)
1 (red)	23.24	38	69	0	1.90
2 (green)	0.07	45	60	45	5.70
3 (blue)	23.24	18	120	90	2.01

attributed to the misalignments of the C-Arm imaging planes, as the C-Arm system was manually oriented.

C. Navigation in Phantom Anatomy

To demonstrate the feasibility of the COAST guidewire motion in anatomical 3D-vasculature, we consider two vascular sections: 1) a high curvature segment of the femoral artery, and 2) the initial curvature of an aortic arch (see Fig. 8(a)-(b)). We use the Vascular Modeling Toolkit (vmtk) to segment each of these blood vessels from anonymized CT data and extract vascular centerlines [29]. We then approximate the centerline points with a cubic spline, for which we compute the Menger curvature at each triad of points along the spline. We identify areas of constant curvature by thresholding the curvature along the centerline length. For a vascular segment of constant radius of curvature, δ, we use singular value decomposition to find the normal to the plane of bending ($\boldsymbol{n}$). This process is then repeated for all the curved and straight portions of the centerline approximation. The torquing angle, ψ, is calculated by finding the angle between normal vectors of consecutive bending planes (see Fig. 8(b)). We then project all the points of a given constant curvature section, onto the bending plane corresponding to normal vector $\boldsymbol{n}$. Finally, we use the Gauss-Newton method to solve a nonlinear least-squares problem iteratively and compute the best fitting circle to the projected points (Gander-Golub-Strebel fit [30]). The cost function to be minimized is the sum of the squares of the distances, $d_i^2 = (\|z - \tilde{\boldsymbol{x}}_{\boldsymbol{i}}\| - r)^2$, z is the center of the circle, $\tilde{\boldsymbol{x}}_{\boldsymbol{i}}$ are the projected 2D points and r is the radius of the circle. Taking $\boldsymbol{u} = (z_1, z_2, r)^T$, the Gauss-Newton method is applied to find $\tilde{\boldsymbol{u}}$, such that quantity, $\Sigma_{i=1}^{m} d_i(\boldsymbol{u})^2$ is minimized. The start and end of the curved centerline are projected on the best fitting circle, and the angle between these points is determined (see θ in Fig. 8(a-b)(inset)). Similarly, the length of the centerline between two consecutive curved segments is used to determine pre-curvature offsets (see a in Fig. 8(a-b)(inset)). Finally, the combined set of parameters $\{a, \delta, \theta, \psi\}$ is used to determine the desired Cartesian-space trajectory as input to the Jacobian-based control scheme.

The 3D-printed phantom models of the aortic bifurcation and aortic arch (Formiga P110 Velocis SLS printer, Bavaria, Germany) were placed under the C-Arm system with the guidewire positioned near the start point of each phantom vasculature (see Fig. 8(c) and 8(c)(inset)). The execution of paths in the femoral artery ($\{8\,\text{mm}, 18.7\,\text{mm}, 108.9^\circ, 0^\circ\}$) and aortic arch ($\{15\,\text{mm}, 40.8\,\text{mm}, 66.35^\circ, -20^\circ\}$) can be seen in Fig. 8(d) and Fig. 8(e), respectively. Fig. 8(d)-(e) show the guidewire tracking the generated trajectories. The position of the tip of

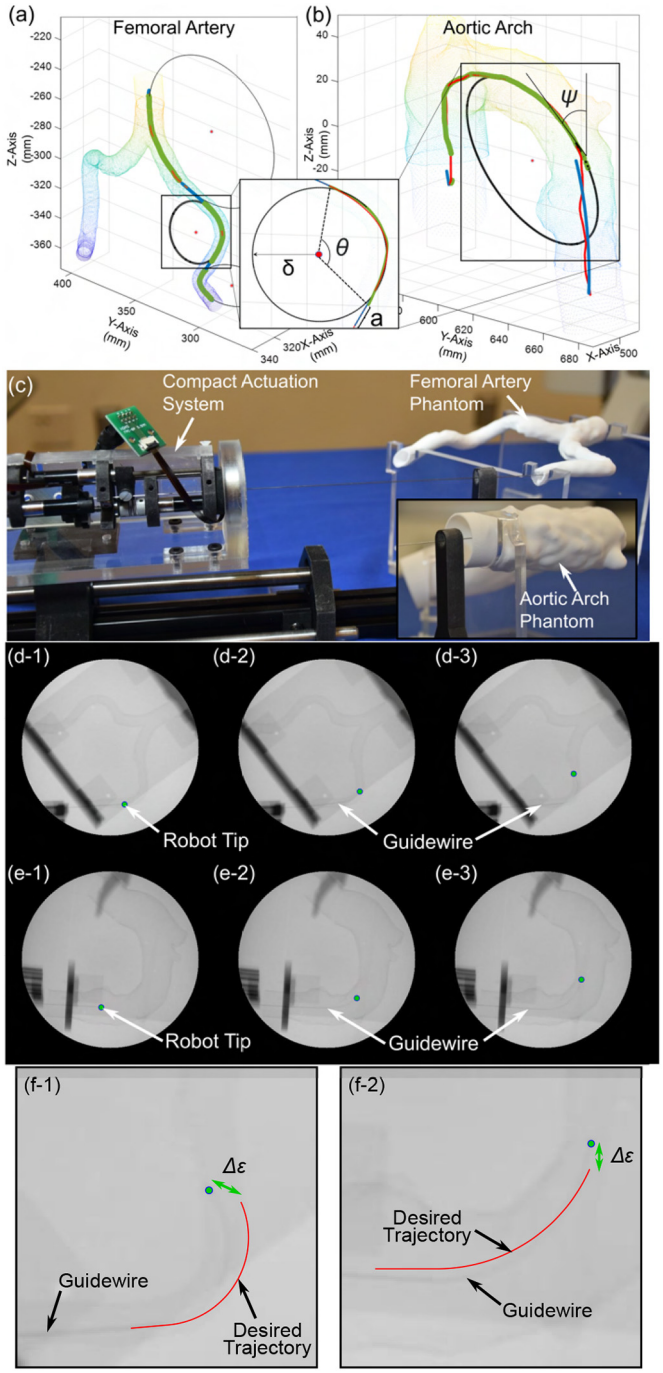

Fig. 8. Extraction of curvatures from vascular centerlines for the (a) femoral artery and (b) aortic arch; (c) Experimental setup; Experimental results shown by fluoroscopy images of guidewire motion for (d-1)-(d-3) a curve in the femoral artery and (e-1)-(e-3) aortic arch; The final positions compared to the desired trajectory for (f-1) the femoral artery and (f-2) the aortic arch.

the guidewire was manually determined from the image data shown in Fig. 8(f-1) for the femoral artery and Fig. 8(f-2) for the aortic arch. The final tip position error for the femoral artery and the aortic arch paths, with respect to the generated trajectories, are estimated as 7.17 mm and 6.55 mm, respectively. The errors are estimated similar to the approach in Section IV-B (0° plane is taken as the horizontal). In addition to the deviations due to coupling, the weight of the tip contributes to the error as it changes the plane of bending and the plane of FTL motion.

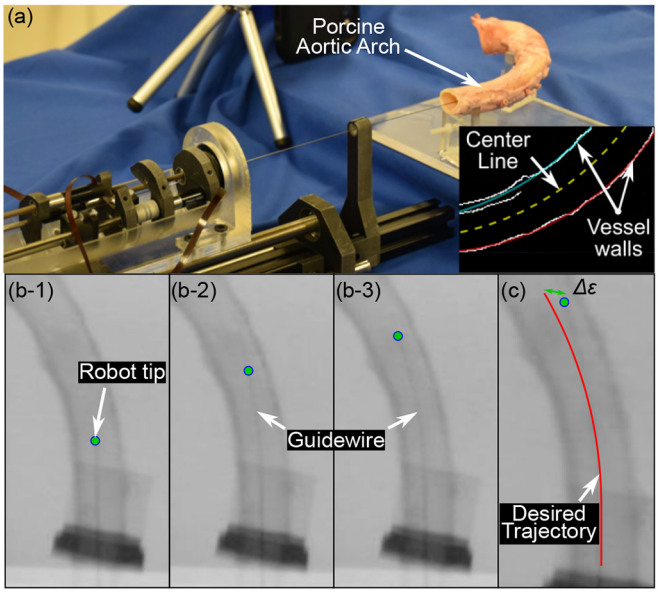

Fig. 9. (a) Experimental setup for porcine aortic arch (inset: curvature extraction for traversed path), (b-1)-(b-3) Fluoroscopy images of guidewire motion for the computed curve within the *ex vivo* animal vasculature, and (c) the final position of the guidewire compared to the desired path.

D. Navigation in ex vivo Porcine Vasculature

To further demonstrate the ability of the COAST guidewire to traverse through vasculature segments, navigation through a porcine aortic arch was conducted as shown in Fig. 9(a). To extract the path within the aortic arch (LAMPIRE Biological Laboratories, Inc., Pipersville, USA), it was placed under the C-arm system and imaged from the top plane. Once scanned, the image of the aorta was thresholded and the vasculature wall boundaries were identified using the Canny edge detection algorithm [31]. The inner wall, though partially identified (see Fig. 9(a)(inset)), was ignored and the radius of curvature of the outer walls of the porcine aorta was determined by fitting constant curvature arcs. The average of the radius of curvature of the two outer walls was approximated to be the radius of curvature of the centerline of the aorta, as shown in Fig. 9(a)(inset). The path to be traversed, characterized by $\{a, \delta, \theta, \psi\}$, was identified to be $\{15\,\text{mm}, 106.3\,\text{mm}, 30°, 90°\}$. Fig. 9(b-1) through Fig. 9(b-3) shows the guidewire executing the trajectory, where the guidewire was observed to stay approximately on the centerline as intended. The tip of the guidewire was manually selected from the image data and the absolute position error of the guidewire tip from the generated trajectory was determined to be 5.61 mm as shown in Fig. 9(c).

Further navigation for secondary and tertiary bending curves in the 3D printed phantom models (Section IV-C) and the porcine vasculature is limited by the plastic deformation of the inner steel tube when the robot is positioned within the curved section after the first FTL maneuver. This deformation prevents the functioning of the inner tube to control the bending length. A nitinol inner tube will be considered in future iterations of the robot to allow more FTL motions and traversal of longer, tortuous sections of vasculature. Effects of blood

flow and vessel wall interactions will also be explored in experimental setups with a pulsatile flow system. A non-invasive X-ray imaging system for real-time tracking and feedback control of the robot for navigation within 3D printed phantoms (Section IV-C) or *ex vivo* animal vasculature will be considered in our future work.

V. Conclusion

In this work, the kinematics of a COaxially Aligned STeerable (COAST) robot guidewire robot were analyzed and utilized to achieve three dimensional follow-the-leader motion with Jacobian-based control. A forward kinematics model is presented and used to derive an overdetermined analytical Jacobian matrix. Velocity kinematics, along with a Jacobian-based control scheme, is then used for Cartesian space trajectory control of the guidewire robot to perform follow-the-leader motion in free space, and within 3D printed phantoms and *ex vivo* animal vasculature. Future work includes extending the control model to include feedback from non-invasive image guidance for the COAST guidewire in constrained vascular anatomy.

Acknowledgment

The authors would like to acknowledge Sharan R. Ravigopal for his assistance in performing experiments with the C-Arm System.

References

[1] S. S. Virani et al., "Heart disease and stroke statistics—2021 update: A report from the american heart association," *Circulation*, vol. 143, no. 8, pp. e254–e743, 2021.

[2] G. Dagnino, J. Liu, M. E. M. K. Abdelaziz, W. Chi, C. Riga, and G.-Z. Yang, "Haptic feedback and dynamic active constraints for robot-assisted endovascular catheterization," in *Proc. IEEE/RSJ Int. Conf. Intell. Robots Syst. (IROS)*, 2018, pp. 1770–1775.

[3] Z. Higgs, D. Macafee, B. Braithwaite, and C. Maxwell-Armstrong, "The Seldinger technique: 50 years on," *Lancet*, vol. 366, no. 9494, pp. 1407–1409, 2005.

[4] S. Macdonald, R. Lee, R. Williams, and G. Stansby, "Towards safer carotid artery stenting," *Stroke*, vol. 40, no. 5, pp. 1698–1703, 2009. [Online]. Available: https://www.ahajournals.org/doi/abs/10.1161/STROKEAHA.109.547117

[5] H. Rafii-Tari, C. J. Payne, and G.-Z. Yang, "Current and emerging robot-assisted endovascular catheterization technologies: A review," *Ann. Biomed. Eng.*, vol. 42, no. 4, pp. 697–715, 2014.

[6] S. Li and G. Hao, "Current trends and prospects in compliant continuum robots: A survey," *Actuators*, vol. 10, no. 7, p. 145, 2021. [Online]. Available: https://www.mdpi.com/2076-0825/10/7/145

[7] A. T. Tung, B.-H. Park, G. Niemeyer, and D. H. Liang, "Laser-machined shape memory alloy actuators for active catheters," *IEEE/ASME Trans. Mechatronics*, vol. 12, no. 4, pp. 439–446, Aug. 2007.

[8] P. E. Dupont, J. Lock, B. Itkowitz, and E. Butler, "Design and control of concentric-tube robots," *IEEE Trans. Robot.*, vol. 26, no. 2, pp. 209–225, Apr. 2010.

[9] R. J. Webster, J. M. Romano, and N. J. Cowan, "Mechanics of precurved-tube continuum robots," *IEEE Trans. Robot.*, vol. 25, no. 1, pp. 67–78, Feb. 2009.

[10] M. F. Rox et al., "Mechatronic design of a two-arm concentric tube robot system for rigid neuroendoscopy," *IEEE/ASME Trans. Mechatronics*, vol. 25, no. 3, pp. 1432–1443, Jun. 2020.

[11] J. Kim, P. B. Nguyen, B. Kang, E. Choi, J.-O. Park, and C.-S. Kim, "A novel tip-positioning control of a magnetically steerable guidewire in sharply curved blood vessel for percutaneous coronary intervention," *Int. J. Control Autom. Syst.*, vol. 17, no. 8, pp. 2069–2082, May 2019.

[12] T. Liu et al., "Iterative jacobian-based inverse kinematics and open-loop control of an MRI-guided magnetically actuated steerable catheter system," *IEEE/ASME Trans. Mechatronics*, vol. 22, no. 4, pp. 1765–1776, Aug. 2017.

[13] Z. Yang, L. Yang, M. Zhang, C. Zhang, S. C. H. Yu, and L. Zhang, "Ultrasound-guided catheterization using a driller-tipped guidewire with combined magnetic navigation and drilling motion," *IEEE/ASME Trans. Mechatronics*, early access, Nov. 4, 2021, doi: 10.1109/TMECH.2021.3121267.

[14] Y. Chitalia, X. Wang, and J. P. Desai, "Design, modeling and control of a 2-DoF robotic guidewire," in *Proc. IEEE Int. Conf. Robot. Autom. (ICRA)*, 2018, pp. 32–37.

[15] T. Kato, I. Okumura, S.-E. Song, A. J. Golby, and N. Hata, "Tendon-driven continuum robot for endoscopic surgery: Preclinical development and validation of a tension propagation model," *IEEE/ASME Trans. Mechatronics*, vol. 20, no. 5, pp. 2252–2263, Oct. 2015.

[16] M. W. Hannan and I. D. Walker, "Kinematics and the implementation of an elephant's trunk manipulator and other continuum style robots," *J. Robot. Syst.*, vol. 20, no. 2, pp. 45–63, 2003.

[17] B. A. Jones and I. D. Walker, "Kinematics for multisection continuum robots," *IEEE Trans. Robot.*, vol. 22, no. 1, pp. 43–55, Feb. 2006.

[18] M. Mahvash and P. E. Dupont, "Stiffness control of surgical continuum manipulators," *IEEE Trans. Robot.*, vol. 27, no. 2, pp. 334–345, Apr. 2011.

[19] M. T. Chikhaoui and J. Burgner-Kahrs, "Control of continuum robots for medical applications: State of the art," in *Proc. 16th Int. Conf. New Actuators (ACTUATOR)*, 2018, pp. 1–11.

[20] J. Lai, K. Huang, B. Lu, Q. Zhao, and H. Chu, "Verticalized-tip trajectory tracking of a 3D-printable soft continuum robot: Enabling surgical blood suction automation," *IEEE/ASME Trans. Mechatronics*, vol. 27, no. 3, pp. 1545–1556, Jun. 2022.

[21] S. Jeong, Y. Chitalia, and J. P. Desai, "Design, modeling, and control of a coaxially aligned steerable (COAST) guidewire robot," *IEEE Robot. Autom. Lett.*, vol. 5, no. 3, pp. 4947–4954, Jul. 2020.

[22] S. R. Ravigopal, T. A. Brumfiel, and J. P. Desai, "Automated motion control of the COAST robotic guidewire under fluoroscopic guidance," in *Proc. Int. Symp. Med. Robot. (ISMR)*, 2021, pp. 1–7.

[23] P. A. York, P. J. Swaney, H. B. Gilbert, and R. J. Webster, "A wrist for needle-sized surgical robots," in *Proc. IEEE Int. Conf. Robot. Autom. (ICRA)*, 2015, pp. 1776–1781.

[24] R. M. Murray, Z. Li, S. S. Sastry, and S. S. Sastry, *A Mathematical Introduction to Robotic Manipulation*. Hoboken, NJ, USA: CRC Press, 1994.

[25] J. J. Craig, *Introduction to Robotics: Mechanics and Control, 3/E*. Upper Saddle River, NJ, USA: Prentice-Hall, 2009.

[26] Y. Chitalia, N. J. Deaton, S. Jeong, N. Rahman, and J. P. Desai, "Towards FBG-based shape sensing for micro-scale and meso-scale continuum robots with large deflection," *IEEE Robot. Autom. Lett.*, vol. 5, no. 2, pp. 1712–1719, Apr. 2020.

[27] H. Wang, X. Wang, W. Yang, and Z. Du, "Design and kinematic modeling of a notch continuum manipulator for laryngeal surgery," *Int. J. Control Autom. Syst.*, vol. 18, no. 11, pp. 2966–2973, 2020.

[28] J. T. Dodge, B. G. Brown, E. L. Bolson, and H. T. Dodge, "Lumen diameter of normal human coronary arteries. Influence of age, sex, anatomic variation, and left ventricular hypertrophy or dilation," *Circulation*, vol. 86, no. 1, pp. 232–246, 1992. [Online]. Available: https://www.ahajournals.org/doi/abs/10.1161/01.CIR.86.1.232

[29] L. Antiga, B. Ene-Iordache, and A. Remuzzi, *Centerline Computation and Geometric Analysis of Branching Tubular Surfaces With Application to Blood Vessel Modeling*, UNION Agency, Brussels, Belgium, Feb 2003.

[30] W. Gander, G. H. Golub, and R. Strebel, "Least-squares fitting of circles and ellipses," *BIT Numer. Math.*, vol. 34, no. 4, pp. 558–578, 1994.

[31] J. Canny, "A computational approach to edge detection," *IEEE Trans. Pattern Anal. Mach. Intell.*, vol. PAMI-8, no. 6, pp. 679–698, Nov. 1986.